

Visualizing Field-free Deterministic Magnetic Switching of all-van der Waals Spin-Orbit Torque System Using Spin Ensembles in Hexagonal Boron Nitride

Xi Zhang^{1,+}, Jingcheng Zhou^{1,+}, Chaowei Hu², Kuangyin Deng³, Chuangtang Wang⁴, Nishkarsh Agarwal⁵, Hanshang Jin⁶, Faris A. Al-Matouq¹, Stelo Xu⁶, Roshan S. Trivedi¹, Senlei Li¹, Sumedh Rathi¹, Hanyi Lu^{7,1}, Zhigang Jiang¹, Valentin Taufour⁶, Robert Hovden^{5,8}, Liuyan Zhao⁴, Ran Cheng^{3,9}, Xiaodong Xu^{2,10}, Jiun-Haw Chu², Chunhui Rita Du^{1,*}, and Hailong Wang^{1,*}

¹School of Physics, Georgia Institute of Technology, Atlanta, Georgia 30332, USA

²Department of Physics, University of Washington, Seattle, Washington 98105, USA

³Department of Electrical and Computer Engineering, University of California, Riverside, California 92521, USA

⁴Department of Physics, University of Michigan, Ann Arbor, Michigan 48109, USA

⁵Department of Materials Science and Engineering, University of Michigan, Ann Arbor, Michigan 48109, USA

⁶Department of Physics and Astronomy, University of California, Davis, California 95616, USA

⁷Department of Physics, University of California, San Diego, La Jolla, California 92093, USA

⁸Applied Physics Program, University of Michigan, Ann Arbor, Michigan 48109, USA

⁹Department of Physics and Astronomy, University of California, Riverside, California 92521, USA

¹⁰Department of Materials Science and Engineering, University of Washington, Seattle, Washington 98105, USA

*Corresponding authors: cdu71@gatech.edu, hwang3021@gatech.edu

⁺These authors contributed equally.

Abstract: Recently, optically active spin defects embedded in van der Waals (vdW) crystals have emerged as a transformative quantum sensing platform to explore cutting-edge materials science and quantum physics. Taking advantage of excellent solid-state integrability, this new class of spin defects can be arranged in controllable nanoscale proximity of target materials in vdW heterostructures, showing great promise for improving spatial resolution and field sensitivity of current sensing technologies. Building on this state-of-the-art measurement platform, here we report hexagonal boron nitride-based quantum imaging of field-free deterministic magnetic switching of room-temperature two-dimensional magnet Fe₃GaTe₂ in an all-vdW spin-orbit torque (SOT) system. By visualizing SOT-driven variations of nanoscale Fe₃GaTe₂ magnetic stray field profile under different conditions, we have revealed how the observed magnetic switching evolves from deterministic to indeterministic behavior due to the interplay between out-of-plane spins, in-plane spins and Joule heating. This understanding, which is otherwise difficult to access by conventional transport measurements, offers valuable insights on material design, testing, and evaluation of next-generation vdW spintronic devices.

Spin-orbit torques (SOTs) have been widely used for developing fast, scalable, and energy-efficient magnetization control in modern spintronic memory devices^{1,2}. The recent flourishing van der Waals (vdW) crystals provide an appealing material playground to design, improve, and revolutionize the conventional SOT technologies³⁻⁶. Potential advantages associated with the emerging two-dimensional (2D) spintronic devices include highly engineerable interfacial conditions, tunable polarization of injected spin currents, convenient material co-integrations, and readily established magnetic vdW proximity, opening new pathways for building ultracompact spin logic circuits with tailored functionalities and hybrid performance^{3,7}. The recently observed out-of-plane spin driven field-free deterministic magnetic switching of a perpendicular vdW magnet is a notable example in this catalog⁸⁻¹¹. The elimination of auxiliary magnetic field(s) is particularly favorable for implementing scalable spin memory applications with reduced energy consumption^{8,10-13}.

Despite the remarkable progress made thus far, ongoing research on unconventional SOT-driven field-free magnetic switching in vdW heterostructures has mainly focused on magneto-transport measurements. These studies are susceptible to thermal, electromigration, and magnetoelastic artifacts⁸⁻¹¹, which can in principle be resolved by nanoscale imaging of magnetization switching details. However, implementation of such cutting-edge imaging technique(s) in all-vdW SOT systems remains an open challenge in the current state-of-the-art. This limitation hinders a comprehensive understanding of the fundamental magnetic switching mechanism and impedes future improvement of the device performance.

Here, we report hexagonal boron nitride (hBN)-based quantum imaging¹⁴⁻¹⁷ of field-free deterministic magnetization switching in $\text{WTe}_2/\text{Fe}_3\text{GaTe}_2/\text{hBN}$ vdW heterostructures. Out-of-plane polarized spin currents are generated by the spin source material WTe_2 with reduced crystallographic symmetry^{8-10,18}, which exerts unconventional SOTs on proximal perpendicular Fe_3GaTe_2 magnetization¹⁰. We show that robust deterministic magnetic switching can be realized in few-layer thick vdW magnet Fe_3GaTe_2 without the assistance of an external magnetic field. Nanoscale magnetic imaging was achieved by utilizing optically active spin defects embedded in the constituent hBN encapsulation layer^{17,19-22}. Using wide-field quantum magnetometry techniques^{14,15}, we directly visualize the microscopic Fe_3GaTe_2 stray field profile as a function of electrical switching currents, revealing systematic evolutions of magnetic domains in response to in-plane and/or out-of-plane polarized spin current injection, which is not accessible by conventional electrical SOT measurements. Our study enriches the current understanding of SOT-induced magnetization dynamics in vdW heterostructures, providing valuable information for future design of energy-efficient 2D spin memory devices. Considering the extensive usage of hBN in preparing vdW nano-electronics^{23,24}, we share the optimism that the demonstrated vdW quantum sensing platform could be extended readily to a broad family of 2D stacking systems, opening new avenues for investigating nanoscale electromagnetic behaviors in 2D quantum matter²⁴.

We first review the vdW heterostructures used in the current study for hBN quantum sensing and electrical transport measurements as illustrated in Fig. 1a. Exfoliated WTe_2 , Fe_3GaTe_2 , and hBN nanoflakes with desirable thicknesses and lateral dimensions are picked up in sequence to form $\text{WTe}_2/\text{Fe}_3\text{GaTe}_2/\text{hBN}$ stacking devices, and then released onto Si/SiO_2 substrates with patterned platinum (Pt) electrodes. The thicknesses of WTe_2 and Fe_3GaTe_2 layers are ~ 10 nm and ~ 7 nm to balance the interfacial spin accumulation and electrical shunting effect (see Supplementary Information Note 1 for details). The hBN encapsulation layer is utilized to prevent sample degradation and serves as a 2D quantum sensing platform as discussed below. It is worth

mentioning that Fe_3GaTe_2 is a recently discovered vdW magnet with a bulk Curie temperature exceeding 350 K^{25–27}. Few-layer-thick Fe_3GaTe_2 shows robust magnetic order with a perpendicular magnetic anisotropy above room temperature (see Supplementary Information Note 2 for details), serving as an ideal material candidate to develop functional vdW spintronic devices for practical applications^{10,25,26}. WTe_2 is the spin source material whose broken crystal symmetry allows generation of out-of-plane polarized spin currents when electrical charge currents flow along its low-symmetry crystallographic axis (a -axis)^{8–10,18}. Figure 1b shows a top-down overview optical microscopy image of a prepared $\text{WTe}_2/\text{Fe}_3\text{GaTe}_2/\text{hBN}$ vdW stacking device (device A), and Fig. 1c shows the cross-sectional high angle annular dark-field scanning transmission electron microscopy (HAADF-STEM) image of the WTe_2 layer in the device viewed along the b -axis confirming the reduced lateral mirror symmetry in the ac -plane. The single crystal WTe_2 layer exhibits lattice spacings of 3.6Å and 7.3Å along the a -axis and c -axis, respectively, with no observable stacking faults.

Next, we move to the discussion of wide-field quantum sensing measurements. Figure 1d illustrates the atomic structure of V_{B}^- centers formed in hBN hexagonal crystal lattice with alternating boron (blue) and nitrogen (green) atoms. Each boron atom vacancy V_{B}^- (red) is surrounded by three nearest-neighbor nitrogen atoms and its energy level structure is shown in Fig. 1e. The negatively charged V_{B}^- defect has an out-of-plane oriented $S = 1$ electron spin featuring the characteristic Zeeman effect induced “three-level” spin system, which can be optically addressed by measuring the spin-dependent photoluminescence (PL)^{17,19,28–30}. By probing the energy splitting between PL peaks corresponding to the $m_s = +1$ and $m_s = -1$ spin state(s), the magnitude of local static magnetic field parallel to the V_{B}^- spin axis can be quantitatively obtained^{14–16}. Figure 1f presents a series of optically detected magnetic resonance (ODMR) spectra of V_{B}^- centers measured under different values of out-of-plane magnetic field B_{ext} . The Zeeman effect separates the $m_s = -1$ and $m_s = +1$ spin state(s) by an energy gap of $2\tilde{\gamma}B_{\text{ext}}$, where $\tilde{\gamma}$ denotes the gyromagnetic ratio of V_{B}^- centers. To achieve nanoscale quantum imaging of Fe_3GaTe_2 nanoflake(s) in the current study, we utilize wide-field quantum magnetometry techniques to detect the fluorescence of V_{B}^- ensembles across the field of view projected on a CMOS camera^{14,15}. Figure 1g shows a magnetic stray field B_s map of the prepared vdW stacking device (device A) measured at 260 K. One can see that the atomically thick (~ 6.3 nm) Fe_3GaTe_2 sample shows robust magnetization, in agreement with the magneto-transport studies^{10,26}. The demonstrated hBN-based quantum imaging platform provides an attractive viewport to investigate microscopic spin behaviors in 2D vdW magnets.

We now present electrical transport measurement results showing field-free deterministic magnetic switching of the perpendicular Fe_3GaTe_2 magnetization. The spin source WTe_2 was theoretically predicted and recently demonstrated as a suitable candidate to generate out-of-plane polarized spin currents due to its reduced lateral mirror symmetry^{8–10,18}. It has a mirror symmetry with respect to the bc -plane but not the ac -plane as shown in Fig. 2a. When an electrical charge current is applied along the low-symmetry crystallographic axis (a -axis) of WTe_2 , the broken symmetry enables generation of spin currents with out-of-plane polarization in addition to the conventional spin Hall effect (Fig. 2b)^{8–10,18}. When an in-plane charge current flows along the high-symmetry axis (b -axis), where the mirror symmetry is preserved in the bc -plane, the spin Hall effect dominates and directions of the electric field, spin currents, and spin polarization are mutually orthogonal as shown in Fig. 2c^{8,18}. In the current work, the specific crystal symmetry of WTe_2 was evaluated by rotational anisotropy second harmonic generation (RA-SHG) measurements that has been shown to be powerful in examining symmetries in crystalline solids^{31–}

³⁴. A typical RA-SHG polar plot of few-layer WTe₂ is presented in Fig. 2d, from which we can identify the *bc* mirror plane with zero SHG intensity, and hence, the crystal *a*-axis that is normal to this mirror plane³⁵.

Figure 2e presents the current driven anomalous Hall loop of the Fe₃GaTe₂ sample without the assistance of an external magnetic field (see Supplementary Information Note 3 for details). The electric current is applied along the low-symmetry axis of WTe₂, and the measurement temperature is 200 K. We observed robust field-free deterministic magnetic switching, where the measured Hall voltage signals of Fe₃GaTe₂ show positive/negative jumps at the critical write current pulses and the terminal magnetic state is determined by the current polarity. The field-free bipolar switching of the perpendicular vdW magnet is attributed to out-of-plane spins injected from WTe₂, which effectively compensate for the local magnetic damping and overcome the anisotropy of proximal Fe₃GaTe₂ magnetization. To confirm the physical picture discussed above, we further measured the shift of anomalous Hall loops of Fe₃GaTe₂ to characterize the effective field produced by the unconventional SOTs from WTe₂. One can see that the measured anomalous Hall loops exhibit a clear shift towards the negative (positive) direction when large positive (negative) electric current pulses ($I_p = \pm 6.5$ mA) are applied along the *a*-axis of WTe₂ as shown in Fig. 2f. Note that the presented anomalous Hall loops become significantly tilted and deviate from the original square shape with a reduced magnetic coercivity due to enhanced Joule heating under higher current applications. The amount of the field shift becomes larger with increasing amplitude of electrical pulse currents and the efficiency of the equivalent out-of-plane magnetic field is characterized to be $\sim 8.1 \times 10^{-6}$ G/(A·cm⁻²), from which the unconventional SOT efficiency is estimated to be 0.070 ± 0.005 in the all-vdW material system (see Supplementary Information Note 4 for details).

In sharp contrast, the signature of field-free deterministic magnetic switching vanishes when electric current pulses are applied along the high-symmetry crystallographic axis (*b*-axis) of WTe₂ as shown in Fig. 2g. Without the assistance of out-of-plane spins or an auxiliary in-plane magnetic field breaking the time reversal symmetry, the Fe₃GaTe₂ magnetization is driven to an intermediate phase that is in-plane magnetized or thermally randomized under both large positive and negative current pulses (see Supplementary Information Note 3 for details). The in-plane antidamping SOT could tilt the Fe₃GaTe₂ magnetization to the sample plane^{8,36} followed by spontaneous out-of-plane self-remagnetization after electrical write current pulses are turned off. Theoretically, the incipient Fe₃GaTe₂ domains equally favor the two magnetic easy states, magnetization pointing up and pointing down, leading to fully randomly oriented magnetic domains without showing a total net perpendicular magnetization⁸. Current-induced Joule heating effect may also be involved in this process by driving thermal demagnetization in the Fe₃GaTe₂ sample, however, the overall “two-step” out-of-plane demagnetization-remagnetization physical picture remains valid due to the lack of a symmetry breaking field to deliver the deterministic perpendicular switching^{8,36}. Note that no notable shift of anomalous Hall loops of the Fe₃GaTe₂ sample is observed when large electric current pulses are applied along the high-symmetry crystallographic axis of WTe₂ as shown in Fig. 2h, corroborating the absence of out-of-plane polarized spin currents.

We now utilize hBN-based wide-field quantum microscopy^{14,15} to visualize the field-free deterministic magnetic switching of Fe₃GaTe₂ at the nanoscale. Figures 3a-3h present a series of representative stray field maps of the Fe₃GaTe₂ sample measured at the corresponding points (“A” to “H”) on the unconventional SOT-driven magnetic hysteresis loop. Electric current pulses I_p are applied along the low-symmetry axis of WTe₂ to ensure the field-free nature of the observed

magnetic switching behavior (Fig. 3i). One can see that the Fe_3GaTe_2 sample starts from one of the spontaneous magnetic easy states with magnetization pointing down, producing a negative stray field in point “A” (see Supplementary Information Notes 5 and 6 for details). When electrical write current pulse I_p is below the threshold value, the measured stray field B_s map basically remains the same, indicating a negligible effect of out-of-plane spins on the Fe_3GaTe_2 magnetization. When ramping I_p above the critical value, the out-of-plane antidamping SOT starts to locally flip the perpendicular Fe_3GaTe_2 magnetization, generating stray field with opposite polarity. The observed field-free magnetic switching starts from incipient magnetic domains at locations where the energy barrier is the lowest and then extends to neighboring Fe_3GaTe_2 sample area as shown in Figs. 3b-3d. When reaching the top plateau value of the anomalous Hall loop, $\sim 70\%$ portion of the Fe_3GaTe_2 magnetic domain has been flipped (Fig. 3d) in absence of an external magnetic field, in agreement with our magneto-transport measurement results. Inverting the electrical write current pulses into the negative regime leads to a reversal of the magnetic switching polarity accompanied by retraction of the flipped Fe_3GaTe_2 magnetic domains (Figs. 3e-3g). Sweeping I_p back to the starting point (“A”) completes the entire anomalous Hall loop, and the measured Fe_3GaTe_2 stray field map is almost identical with that measured in the initial magnetic state. The presented hBN wide-field quantum imaging measurements directly visualize the out-of-plane spin driven field-free deterministic magnetic switching of an atomically thick perpendicular vdW magnet, revealing SOT-induced nanoscale domain wall nucleation and propagation on 2D flatland. Note that we also visualized field-free full magnetic switching in other Fe_3GaTe_2 samples, and the observed switching ratio is sensitive to variations of magnetic inhomogeneities/defects and dimensions of prepared vdW devices (see Supplementary Information Notes 7 and 8 for details).

Achieving deterministic and nonvolatile magnetization control constitutes a key challenge for developing modern spintronic memory and computation technologies^{1,2}. Next, we utilize hBN-based wide-field quantum magnetometry techniques to evaluate the (in)deterministic nature of presented field-free control of Fe_3GaTe_2 magnetization. Figure 4a shows the “step-like” variations of anomalous Hall signals of the Fe_3GaTe_2 sample in response to a train of positive and negative current pulses, $I_p = \pm 6.5$ mA, applied along the a -axis of WTe_2 . Robust deterministic magnetization switching feature is highlighted in a series of wide-field quantum images recorded after individual current pulse applications as presented Fig. 4b. One can see that the positive and negative large current pulses reliably switch the Fe_3GaTe_2 magnetic domains between two deterministic states, from magnetization up to magnetization down or vice versa, in agreement with the “step-like” variations of anomalous Hall signals shown in the bottom panel of Fig. 4a. When I_p is increased to ± 8.5 mA, the magneto-transport results basically remain the same as shown in Fig. 4c. However, a microscopic view provided by our quantum imaging measurements indicates that the observed magnetic switching of Fe_3GaTe_2 has already deviated from the perfect deterministic nature. A small portion of the Fe_3GaTe_2 magnetic domains cannot be switched reproducibly between the two magnetic easy states. Although field-free deterministic magnetic switching still dictates most of the Fe_3GaTe_2 magnetization, it is evident that some local magnetic patterns show random variations after every electrical writing cycle [Fig. 4(d)]. The observed experimental feature is attributable to current induced Joule heating effect, which introduces random demagnetization-remagnetization behavior at certain Fe_3GaTe_2 sample areas where the local transient temperature is driven above the Curie point under large current pulse applications.

The deterministic magnetization control disappears when I_p is applied along the b -axis of WTe_2 . Figure 4f presents the evolution of Fe_3GaTe_2 magnetic stray field maps in response to the

positive and negative pulse current train ($I_p = \pm 6.5$ mA) applied along the high-symmetry b -axis of WTe_2 . In this case, fully randomly oriented magnetic domains are spontaneously formed over the entire Fe_3GaTe_2 sample area with a net out-of-plane magnetization approximately to zero due to the absence of out-of-plane spins injected from WTe_2 . While the measured anomalous Hall signals basically fluctuate around the zero value with little variations (Fig. 4e, bottom), hBN quantum imaging reveals that the microscopic Fe_3GaTe_2 magnetic patterns have dramatically changed at the nanoscale during the indeterministic magnetization control process (see Supplementary Information Note 7 for details).

In summary, we have demonstrated hBN-based wide-field quantum imaging of field-free deterministic magnetic switching in a room-temperature 2D magnet. Current-induced nanoscale nucleation and evolution of magnetic domains in atomically thick Fe_3GaTe_2 are visualized by V_B^- spin ensembles contained in the hBN encapsulation layer. We further reveal how the observed magnetic switching evolves from deterministic to indeterministic behavior due to the interplay between out-of-plane spins, in-plane spins, and Joule heating effects. Our wide-field imaging results show that the Fe_3GaTe_2 sample reliably switches between two deterministic magnetic states when current pulses are applied along the low-symmetry crystallographic axis of the spin source material WTe_2 . The deterministic nature of the field-free magnetic switching starts to degenerate when the magnitude of the electrical write current is above a certain threshold value due to involvement of local thermal heating effect. The deterministic magnetic switching feature is clearly absent when electric current pulses are applied along the high-symmetry crystallographic axis of WTe_2 . Our study sheds light on the microscopic details of unconventional SOT-driven magnetization dynamics, providing insights into future design, integration, and engineering of 2D spintronic devices. We expect that the recently discovered room-temperature vdW magnet Fe_3GaTe_2 will serve as a promising building block for this purpose^{10,25–27}. The presented hBN-based vdW quantum sensing platform further opens new opportunities for exploring nanoscale spin transport and dynamic behaviors in a broad family of miniaturized 2D heterostructure systems^{3,19,23,24}.

Data availability. All data supporting the findings of this study are available from the corresponding author(s) on reasonable request.

Acknowledgements. This work was primarily supported by the U.S. Department of Energy (DOE), Office of Science, Basic Energy Sciences (BES), under award No. DE-SC0024870. J. Z. acknowledges the support from the U.S. National Science Foundation under award No. DMR-2342569. H. L. was supported by the Air Force Office of Scientific Research (AFOSR) under award No. FA9550-21-1-0125. C. R. D. also acknowledges the support from the Office of Naval Research (ONR) under grant No. N00014-23-1-2146. The growth and characterization of Fe_3GaTe_2 single crystals were supported by the Center on Programmable Quantum Materials, an Energy Frontier Research Center funded by the U.S. Department of Energy (DOE), Office of Science, Basic Energy Sciences (BES), under award No. DE-SC0019443. K. D. and R. C. were supported by the U.S. National Science Foundation under Award No. DMR-2339315. L. Z. acknowledges the support from the U.S. Department of Energy (DOE), Office of Science, Basic Energy Science (BES), under award No. DE-SC0024145. R. H. and N. A. acknowledge support from the National Science Foundation through the Materials Research Science and Engineering Center at the University of Michigan, Award No. DMR-2309029. The synthesis of WTe_2 crystals

was supported by the UC Lab Fees Research Program (grant No. LFR-20-653926). The synthesis of ^{10}B -enriched monoisotopic hBN crystals was supported by NASA-CLEVER SSERVI (CAN no. 80NSSC23M0229) and NASA-MSFC (CAN no. 80NSSC21M0271).

Author contributions. X. Z. performed the quantum sensing measurements and analyzed the data with J. Z., S. L., and H. L. J. Z. prepared the vdW stacking devices and performed electrical transport measurements. C. H. grew and characterized bulk Fe_3GaTe_2 crystals under the supervision of X. X. and J.-H. C. K. D. and R. C. contributed to theoretical input and discussions. C. W. performed the second harmonic generation measurements under the supervision of L. Z. N. A. performed the TEM characterizations under the supervision of R. H. H. J., S. X., and V. T. provided WTe_2 crystals. F. A. A., R. S. T., S. R., and Z. J. provided monoisotopic hBN crystals. C. R. D. and H. L. W. supervised this project.

Competing interests

The authors declare no competing interests.

References

1. Manchon, A. *et al.* Current-induced spin-orbit torques in ferromagnetic and antiferromagnetic systems. *Rev. Mod. Phys.* **91**, 035004 (2019).
2. Liu, L. *et al.* Spin-Torque Switching with the Giant Spin Hall Effect of Tantalum. *Science* **336**, 555–558 (2012).
3. Yang, H. *et al.* Two-dimensional materials prospects for non-volatile spintronic memories. *Nature* **606**, 663–673 (2022).
4. Burch, K. S., Mandrus, D. & Park, J.-G. Magnetism in two-dimensional van der Waals materials. *Nature* **563**, 47–52 (2018).
5. Samarth, N. Magnetism in flatland. *Nature* **546**, 216–217 (2017).
6. Thiel, L. *et al.* Probing magnetism in 2D materials at the nanoscale with single-spin microscopy. *Science* **364**, 973–976 (2019).
7. Avsar, A. *et al.* Colloquium: Spintronics in graphene and other two-dimensional materials. *Rev. Mod. Phys.* **92**, 021003 (2020).
8. Kao, I.-H. *et al.* Deterministic switching of a perpendicularly polarized magnet using unconventional spin-orbit torques in WTe₂. *Nat. Mater.* **21**, 1029–1034 (2022).
9. Shin, I. *et al.* Spin-Orbit Torque Switching in an All-Van der Waals Heterostructure. *Adv. Mater.* **34**, 2101730 (2022).
10. Kajale, S. N., Nguyen, T., Hung, N. T., Li, M. & Sarkar, D. Field-free deterministic switching of all-van der Waals spin-orbit torque system above room temperature. *Sci. Adv.* **10**, eadk8669 (2024).
11. Zhang, Y. *et al.* Robust Field-Free Switching Using Large Unconventional Spin-Orbit Torque in an All-Van der Waals Heterostructure. *Adv. Mater.* **36**, 2406464 (2024).
12. Liu, Y. *et al.* Field-free switching of perpendicular magnetization at room temperature using out-of-plane spins from TaIrTe₄. *Nat. Electron.* **6**, 732–738 (2023).
13. Zhang, Y. *et al.* Room temperature field-free switching of perpendicular magnetization through spin-orbit torque originating from low-symmetry type II Weyl semimetal. *Sci. Adv.* **9**, eadg9819 (2023).
14. Huang, M. *et al.* Wide field imaging of van der Waals ferromagnet Fe₃GeTe₂ by spin defects in hexagonal boron nitride. *Nat. Commun.* **13**, 5369 (2022).
15. Healey, A. J. *et al.* Quantum microscopy with van der Waals heterostructures. *Nat. Phys.* **19**, 87–91 (2023).
16. Kumar, P. *et al.* Magnetic Imaging with Spin Defects in Hexagonal Boron Nitride. *Phys. Rev. Appl.* **18**, L061002 (2022).
17. Vaidya, S., Gao, X., Dikshit, S., Aharonovich, I. & Li, T. Quantum sensing and imaging with spin defects in hexagonal boron nitride. *Adv. Phys. X* **8**, 2206049 (2023).
18. MacNeill, D. *et al.* Control of spin-orbit torques through crystal symmetry in WTe₂/ferromagnet bilayers. *Nat. Phys.* **13**, 300–305 (2017).
19. Gottscholl, A. *et al.* Initialization and read-out of intrinsic spin defects in a van der Waals crystal at room temperature. *Nat. Mater.* **19**, 540–545 (2020).
20. Lyu, X. *et al.* Strain Quantum Sensing with Spin Defects in Hexagonal Boron Nitride. *Nano Lett.* **22**, 6553–6559 (2022).
21. Mathur, N. *et al.* Excited-state spin-resonance spectroscopy of V_B defect centers in hexagonal boron nitride. *Nat. Commun.* **13**, 3233 (2022).
22. Gong, R. *et al.* Coherent dynamics of strongly interacting electronic spin defects in hexagonal boron nitride. *Nat. Commun.* **14**, 3299 (2023).

23. Dean, C. R. *et al.* Boron nitride substrates for high-quality graphene electronics. *Nat. Nanotechnol.* **5**, 722–726 (2010).
24. Geim, A. K. & Grigorieva, I. V. Van der Waals heterostructures. *Nature* **499**, 419–425 (2013).
25. Zhang, G. *et al.* Above-room-temperature strong intrinsic ferromagnetism in 2D van der Waals Fe_3GaTe_2 with large perpendicular magnetic anisotropy. *Nat. Commun.* **13**, 5067 (2022).
26. Kajale, S. N. *et al.* Current-induced switching of a van der Waals ferromagnet at room temperature. *Nat. Commun.* **15**, 1485 (2024).
27. Wu, H. *et al.* Spectral evidence for local-moment ferromagnetism in the van der Waals metals Fe_3GaTe_2 and Fe_3GeTe_2 . *Phys. Rev. B* **109**, 104410 (2024).
28. Zhou, J. *et al.* Sensing spin wave excitations by spin defects in few-layer-thick hexagonal boron nitride. *Sci. Adv.* **10**, eadk8495 (2024).
29. Das, S. *et al.* Quantum Sensing of Spin Dynamics Using Boron-Vacancy Centers in Hexagonal Boron Nitride. *Phys. Rev. Lett.* **133**, 166704 (2024).
30. Zang, H.-X. *et al.* Detecting and Imaging of Magnons at Nanoscale with van der Waals Quantum Sensor. *Adv. Funct. Mater.* **35**, 2412166 (2025).
31. Jin, W. *et al.* Observation of a ferro-rotational order coupled with second-order nonlinear optical fields. *Nat. Phys.* **16**, 42–46 (2020).
32. Luo, X. *et al.* Ultrafast Modulations and Detection of a Ferro-Rotational Charge Density Wave Using Time-Resolved Electric Quadrupole Second Harmonic Generation. *Phys. Rev. Lett.* **127**, 126401 (2021).
33. Ahn, Y. *et al.* Electric quadrupole second-harmonic generation revealing dual magnetic orders in a magnetic Weyl semimetal. *Nat. Photonics* **18**, 26–31 (2024).
34. Guo, X. *et al.* Extraordinary phase transition revealed in a van der Waals antiferromagnet. *Nat. Commun.* **15**, 6472 (2024).
35. Drueke, E., Yang, J. & Zhao, L. Observation of strong and anisotropic nonlinear optical effects through polarization-resolved optical spectroscopy in the type-II Weyl semimetal $T_d\text{-WTe}_2$. *Phys. Rev. B* **104**, 064304 (2021).
36. Liu, L., Lee, O. J., Gudmundsen, T. J., Ralph, D. C. & Buhrman, R. A. Current-Induced Switching of Perpendicularly Magnetized Magnetic Layers Using Spin Torque from the Spin Hall Effect. *Phys. Rev. Lett.* **109**, 096602 (2012).

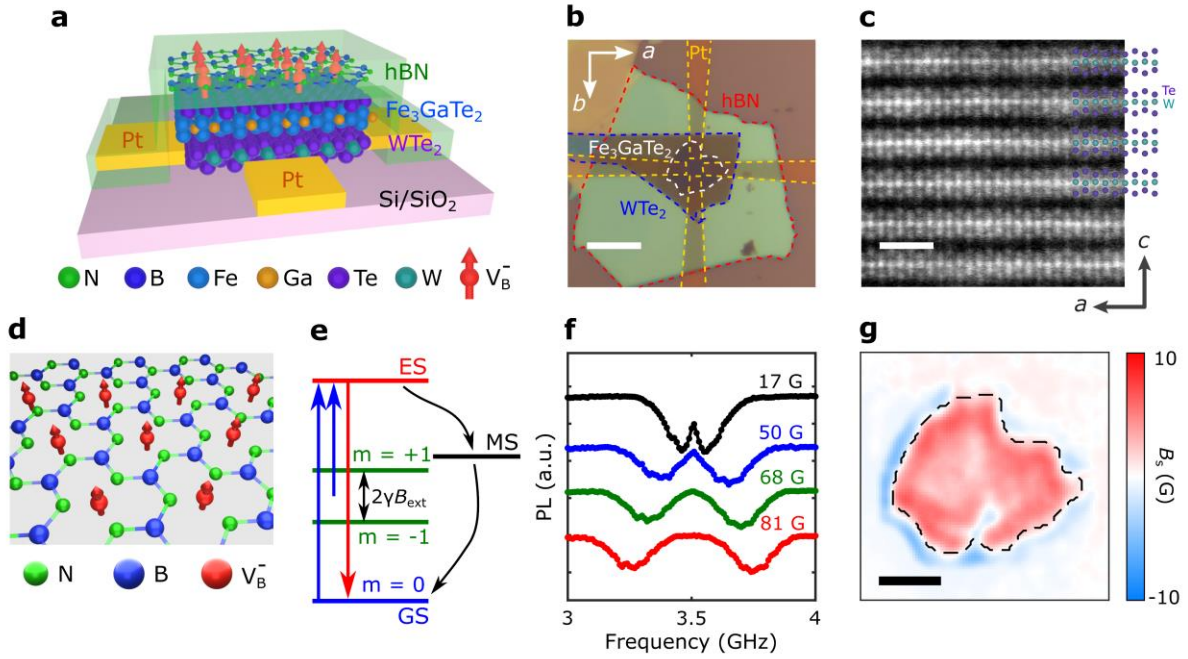


Figure 1. Device structure and hBN-based wide-field quantum imaging platform. **a.** Schematic of the $\text{WTe}_2/\text{Fe}_3\text{GaTe}_2/\text{hBN}$ vdW heterostructure for quantum imaging and electrical SOT switching measurements. **b** Optical microscopy image of a prepared $\text{WTe}_2/\text{Fe}_3\text{GaTe}_2/\text{hBN}$ device. The boundaries of constituent vdW layers are outlined by red (hBN), blue (WTe_2), and white (Fe_3GaTe_2) dashed lines. Pt electrodes are highlighted by yellow dashed lines. The scale bar is $10\ \mu\text{m}$. **c** Cross-sectional HAADF-STEM image of a prepared device viewed along the b -axis of WTe_2 . The highlighted atomic structure shows the broken lateral mirror symmetry in the ac -plane of WTe_2 . The scale bar is $1\ \text{nm}$. **d** V_B^- spin defects (red arrows) formed in the hexagonal crystal structure with alternating boron (blue) and nitrogen (green) atoms. **e** Energy level diagram of a V_B^- spin defect and optical excitation (blue arrow), radiative recombination (red arrow), and nonradiative decay (black arrow) between the ground state (GS), excited state (ES), and metastable state (MS). **f** A series of V_B^- ODMR spectra measured at different values of a perpendicular magnetic field. **g** A stray field map of the Fe_3GaTe_2 sample measured at $260\ \text{K}$ with an external perpendicular magnetic field B_{ext} of $30\ \text{G}$. Black dashed lines outline the boundary of the Fe_3GaTe_2 flake, consistent with the device details shown in Fig. 1b. The scale bar is $4\ \mu\text{m}$.

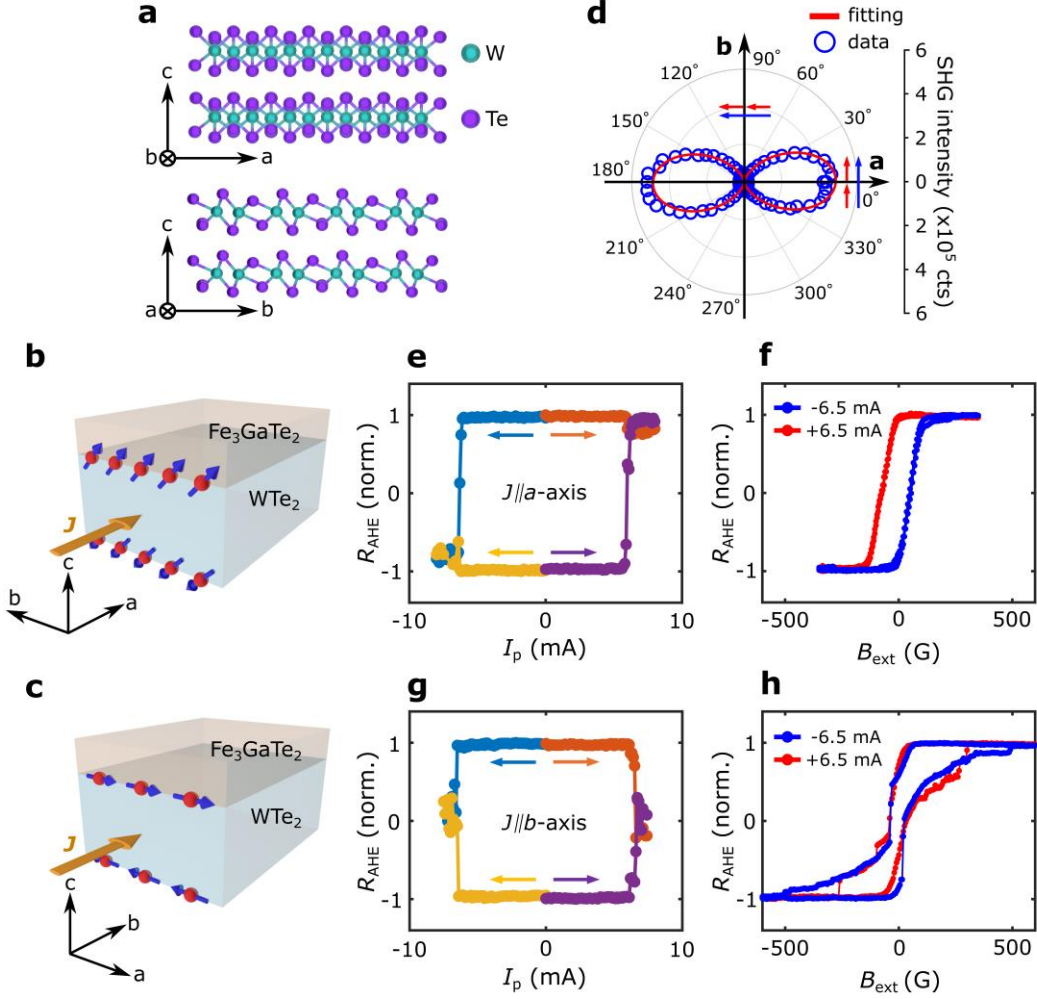


Figure 2. Field-free deterministic and indeterministic magnetic switching in WTe₂/Fe₃GaTe₂/hBN. **a** Atomic arrangement of WTe₂ viewed along its *b*-axis (top) and *a*-axis (bottom) directions. **b, c** Generation of out-of-plane and in-plane polarized spin currents when an electrical charge current *J* flows along the low-symmetry and high-symmetry crystallographic axes of WTe₂. **d** An azimuthal angle dependent SHG pattern in parallel channel characterizing the reduced crystal symmetry in the *ac*-plane of WTe₂. The fitting is based on the electric-dipole SHG response under the *m* point group. Red and blue arrows indicate the polarizations of incident and reflected light at the 0° and 90°, respectively. **e, g** Normalized anomalous Hall resistance of Fe₃GaTe₂ measured as a function of electrical write current pulse *I_p* applied along the *a*-axis (**e**) and *b*-axis (**g**) of WTe₂. The magnitude of *I_p* was increased from zero with the sweeping direction indicated by the color arrows. Fe₃GaTe₂ was initialized to the *m_z* = 1 or *m_z* = -1 state in the beginning of each sweep sequence. External auxiliary magnetic fields were absent in the presented SOT measurements. **f, h** Variations of measured Fe₃GaTe₂ anomalous Hall loops in response to positive and negative electric current pulses (*I_p* = 6.5 mA) applied along the *a*-axis (**f**) and *b*-axis (**h**) of WTe₂. The presented magneto-transport measurements were performed at 200 K.

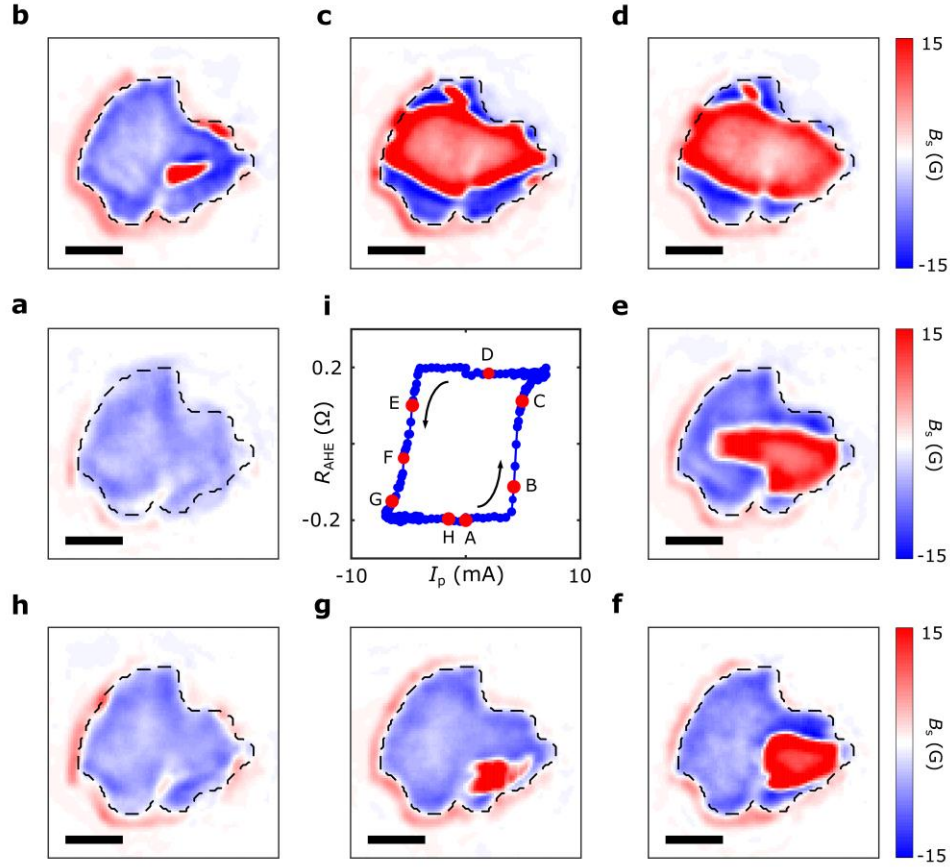


Figure 3. Visualizing field-free deterministic magnetic switching of Fe_3GaTe_2 . a-h hBN-based quantum imaging of microscopic evolutions of Fe_3GaTe_2 magnetic domains during the field-free deterministic magnetic switching process. The scale bar is $4 \mu\text{m}$. i Anomalous Hall resistance of Fe_3GaTe_2 measured as a function of electrical write current pulse I_p in absence of an external magnetic field. The arrows indicate that I_p was swept from zero following the counterclockwise direction around the hysteresis loop and finally returned to the starting point. hBN-based quantum imaging measurements presented in Figs. 3a-3h were performed at the corresponding points from “A” to “H” marked on the field-free deterministic switching loop (Fig. 3i). The SOT-driven magnetic switching and quantum sensing measurements were performed at 260 K.

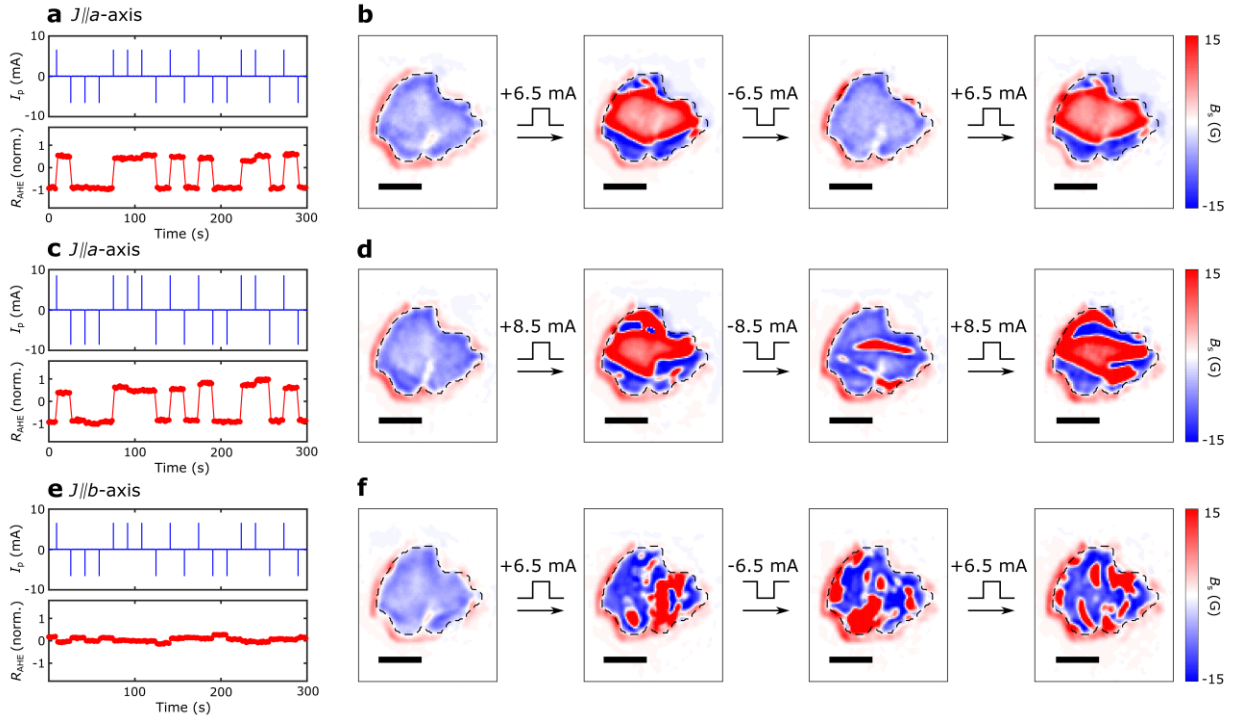


Figure 4. Evaluating (in)deterministic nature of field-free magnetization control of Fe_3GaTe_2 . **a, c** Deterministic magnetic switching of Fe_3GaTe_2 using a train of positive and negative electric current pulses (I_p) with a magnitude of 6.5 mA (**a**) and 8.5 mA (**c**) applied along the a -axis of WTe_2 . **b, d** Variations of magnetic stray field patterns of the Fe_3GaTe_2 sample after individual electric current pulse applications along the a -axis of WTe_2 for $I_p = \pm 6.5\text{mA}$ (**b**) and $\pm 8.5\text{mA}$ (**d**). **e, f** Electrical SOT measurements and the corresponding quantum imaging results for a series of current pulses (I_p) with a magnitude of $\pm 6.5\text{mA}$ applied along the b -axis of WTe_2 . Scale bar is $5\ \mu\text{m}$ in all figures. The SOT-driven magnetic switching and quantum sensing measurements were performed at 260 K.